Reflection characteristics of linear carbon dioxide transition layers

Julián L. Gómez[1] and Claudia L. Ravazzoli[1]

ABSTRACT

Seismic monitoring of underground CO_2 accumulations is a subject of growing interest in applied geophysics. Due to their large impedance contrasts, attention is focused on accumulations of high CO_2 saturation in most cases. However, low-saturation zones with dispersed carbon dioxide, or saturation transition layers, may have an important role in the propagation of waves within the reservoir, giving rise to amplitude and phase changes of the seismic signals. With this motivation, we studied the reflectivity response of a simple reservoir model with a given CO_2 saturation-depth profile, on a theoretical basis. We investigated the influence of the overall saturation, vertical extent, and spatial fluid distribution of a carbon dioxide transition zone in the reflectivity of a reservoir. The parametric analysis entails the computation of the generalized P-wave reflection coefficient and its variations with ray angle (AVA) and frequency (AVF). The combined analysis of AVA and AVF can help to characterize and monitor CO_2 transition layers within geological storage sites.

INTRODUCTION

Man-made CO_2 released into the atmosphere, as is well known, is a significant contributor to the global warming greenhouse effect (White, 2009). As a strategy to reduce these industrial CO_2 emissions, carbon dioxide capture and storage (CCS) projects are being tested and developed worldwide. To evaluate the storage performance and integrity of the CO_2 repositories, such as depleted hydrocarbon reservoirs and saline aquifers, it is mandatory to monitor the presence and distribution of the injected CO_2. The migration of CO_2 within the reservoir after the injection is generally controlled by buoyancy effects and pressure gradients. However, it also depends on rock permeability and porosity, the location of seals, the properties of the CO_2, and the reservoir fluids as well. In addition, the spatial heterogeneity in the transport properties of the reservoir rocks at very small scales may induce irregular distributions of the fluids, giving rise to patchy-saturation patterns. All these factors may result in strongly variable CO_2 saturations within the repository, which, in turn, give rise to spatial variations in the acoustic properties of the medium.

The seismic monitoring of the injected CO_2 is usually limited to the study of the characteristics of the large amplitude seismic reflections coming from high saturation accumulations, due to their good signal-to-noise ratio. Nevertheless, low-saturation zones of diffuse CO_2 have an important role in the propagation of waves within the reservoir, in the study of velocity push-down effects and also in the estimation of the total CO_2 volume stored in the reservoir (Chadwick et al., 2005). Thus, the characterization of zones with CO_2 saturation varying with depth, hereafter referred to as CO_2 saturation transition layers, is a very important task in monitoring studies which has not yet received much attention from the geophysical community.

The reflectivity of transition layers was treated in the work of Wolf (1937). In this classic article, the analytical expression for the reflection coefficient of normal incidence P-waves was derived assuming constant density and a linear trend in velocity with depth. Later, Bortfeld (1960), under the same assumptions as Wolf (1937), derived the same result by considering the transition layer as the limit of a sequence of constant-velocity layers. The reflectivity and amplitude characteristics of reflections from sets of multiple transition layers have been treated theoretically in the work of Berryman et al. (1958). Wuenschel (1960) employed transition layers to test and validate a synthetic seismogram computer code. In his algorithm, a matrix recursive scheme similar to the one used in the present paper, was employed to obtain the reflection coefficient. In the work of Gupta (1966), the problem of the reflectivity from transition layers is numerically extended to consider the case of arbitrary variations of velocity and density, as well as variable angle of incidence. Justice and Zuba (1986) tackle the problem

of the seismic characterization, detectability, and parameter estimation associated to the reflections arising from transition layers in permafrost. More recently, Liner and Bodmann (2010) explored the frequency-dependent nature of the reflectivity from a linear-velocity transition layer, with the aim of detecting its signature in real field data. As pointed out by these authors, the use of spectral analysis allows us to study the frequency-dependent behavior of seismic reflections, giving additional information for data interpretation.

The lack of specific studies about the characteristics of seismic reflections associated with CO_2 transition layers encouraged us to examine the behavior of their associated generalized reflectivity for variable ray angle (AVA) and frequency (AVF). We focus attention on the vertical variations in CO_2 saturation for a given linear saturation-depth profile within a simple geologic reservoir. The reservoir reflectivity response is obtained using a matrix propagator method for layered elastic media.

We characterize the AVA/AVF response of the transition for variable CO_2 saturation, fluid mixture type, and thickness, which can be useful as detection tools for CO_2 monitoring. Our results show that carbon dioxide transition layers behave differently from classical linear-velocity transition zones or constant CO_2 layers, due to the nonlinear effect of CO_2 in the elastic parameters of the rocks.

The paper is organized as follows. First, we review the modeling procedure and give a description of our CO_2 transition layered model. Next, we perform a reflectivity AVA/AVF analysis based on a simple reservoir scenario. In this analysis, we model and discuss the impact on the reservoir reflectivity of the partial bulk CO_2 saturation, transition thickness, and fluid mixture distribution type. Finally, an inspection of the differences and similarities among the studied transition, a constant CO_2 saturation profile, and a linear-velocity transition zone (Wolf ramp) is also given. In the appendices, the derivation of the normal incidence reflection coefficient of the Wolf ramp is included.

MODELING PROCEDURE

As defined by Wolf (1937), transition layers are zones where the elastic constants of the rocks are continuous functions of position. Transition layers of constant density and linear-velocity trend with depth, termed as Wolf ramps, have been studied in the geophysical literature omitting the analysis of the rock-physics parameters responsible for their generation. In this work, we will consider a transition layer that is generated by the depth variation of the CO_2 saturation in a reservoir's pore space originally saturated with brine. This vertical change in carbon dioxide content will induce a transition of nonlinear velocity trend. We assume that the migration of CO_2 is mainly controlled by buoyancy and that the reservoir permeability is homogeneous and isotropic, resulting in a laterally constant CO_2 saturation field. The elastic properties of the rocks for the different partial saturation states are computed using a traditional rock-physics fluid substitution procedure. So, it is assumed that no chemical reaction takes place between the rock matrix and its pore fluids. Because solubility effects of CO_2 in brine are negligible (Batzle and Wang, 1992), they are not considered within the scope of the present paper. The mechanical properties of the saturated rocks are modeled assuming that the rock matrix and the pore fluids move in phase. Then, by defining an effective bulk modulus for the multiphase fluids, the bulk modulus of the saturated rock can

be obtained using the formulation of Gassmann (1951), which is strictly valid only when the pore fluids are mixed uniformly at very small scales (Mavko and Mukerji, 1998). In case the CO_2 generates patches of arbitrary geometry within the brine-saturated rock, the effective elastic modulus of the reservoir rock can be estimated using Hill's modulus in the form given by Mavko and Mukerji (1998). Taking into account the significant differences between the Gassmann and Hill velocity estimations and due to the uncertainties in the knowledge of the in situ CO_2-to-brine distribution, we assume that, for each saturation, it is reasonable to compute the average between both velocities. The density and bulk modulus of CO_2 for the given reservoir temperature and pressure conditions are computed using the Peng and Robinson (1976) two-parameter equation of state for real fluids, while those of brine are taken from Chadwick et al. (2005).

To calculate the reflectivity of the model, we use a matrix propagator method. This approach is based on the continuity of particle displacements and stress components at the interfaces between sets of plane layers embedded between two half-spaces. The resulting equations take the form of a recursive algorithm that allows the computation of the generalized complex reflection and transmission coefficients of the multilayer model (Tsvankin, 1995; Brekhovskik, 1980). From the physical and geometrical parameters of each layer, the propagator matrix is computed in the form,

$$\mathcal{P} = \prod_{k=1}^{n} \mathcal{M}_k(V_P^k, V_S^k, \rho_b^k, h^k; f, \theta). \tag{1}$$

In this formula, $\mathcal{M}_k$ is a 4×4 matrix that depends on seismic velocities V_P^k and V_S^k, bulk density ρ_b^k, and thickness h^k of layer k, n being the number of layers in the model. It is also a function of wave frequency f and incidence angle θ of an incident monochromatic plane compressional P-wave. Given the reservoir propagator matrix $\mathcal{P}$ from equation 1 and given the displacement-stress vector at the half-spaces $\mathcal{A}^T = [u_x, u_z, \tau_{zz}, \tau_{zx}]$ (where T denotes the transpose) from the continuity of the displacements u_x and u_z and the stresses τ_{zz} and τ_{zx} across the model, we have

$$\mathcal{A}_{n+1} = \mathcal{P}\mathcal{A}_0. \tag{2}$$

Here, $\mathcal{A}_0$ and $\mathcal{A}_{n+1}$ are the corresponding displacement-stress vectors at the top and bottom half-spaces, respectively. From equation 2, we can obtain the generalized complex potential reflection coefficients for P-waves, denoted as $R_{pp}(f, \theta)$. To solve this system directly in terms of the potential amplitudes, we first write the displacement-stress vectors as functions of the displacement Helmholtz's potentials, $\mathbf{u} = \nabla\Phi + \nabla\times\boldsymbol{\psi}$, where Φ is the potential associated with P-waves and $\boldsymbol{\psi}$, the potential associated with SV-waves. For a plane wave, these potentials have an expression that is linear in their amplitudes, e.g., $\Phi = A \exp i(k_x x - k_z z - \omega t) + B \exp i(k_x x + k_z z - \omega t)$ for the P-wave in the first half-space. Here, A and B are the amplitudes of the incident and reflected waves, respectively, and i is the imaginary unit. Once the system is solved, we can obtain the P-wave reflection coefficient from the related potential amplitudes, in this case $B/A = R_{pp}(f, \theta)$.

Our aim is to calculate and analyze the reflectivity response of the medium with a given vertical distribution of CO_2. In response to the lack of detailed information in geophysical literature about carbon dioxide vertical saturation profiles, we propose a simple but insightful linear saturation trend. This profile is inspired by the axisymmetric flow simulations presented by Chadwick et al. (2006) for

Utsira sandstone, which show that high CO_2 accumulation zones are followed by a progressive decline in saturation with depth.

We consider a saturation profile $S_{CO_2}(z)$, where z is depth, defined as $z \geq 0$ ($z = 0$ at the top of the transition) and given by a piecewise linear function that satisfies

$$\frac{1}{h}\int_0^h S_{CO_2}(z)dz = \bar{S} \quad \text{and} \quad S_{CO_2}(z \geq h) = 0, \quad (3)$$

where h is the thickness of the transition layer (see Figure 1) and $\bar{S}$ is its bulk CO_2 saturation. So, for $0 \leq z \leq h$, we can write

$$S_{CO_2}(z) = 2\bar{S}\left(1 - \frac{z}{h}\right). \quad (4)$$

Using equation 4 for the given $\bar{S}$ and h, and as long as $\bar{S} \leq 50\%$, we can independently analyze the effects related to the bulk amount of CO_2 and layer thickness. It must be noted that, in addition to the simple linear saturation-depth model, we also tested other similar profile shapes with the same bulk properties, but their reflectivity showed small differences that do not affect or limit the scope of the conclusions.

To complete the description of the modeling procedure, we recall that the existence of an heterogeneous fluid distribution may give rise to mesoscopic wave attenuation and velocity dispersion phenomena in the seismic frequency range. There are many studies about the numerical modeling of these effects (Dutta and Odé, 1979; Pride et al., 2004; Rubino et al., 2009), which are strongly dependent on the shapes and characteristic lengths of the patches. Because these parameters are rarely known, we avoid dealing with this uncertainty in our analysis by assuming elastic layers where no attenuation-dispersion phenomena, associated with the patchy fluid distribution or the vertical variation in CO_2 saturation, take place. However, these effects can be easily included in our formulation using viscoelastic constitutive relations in the frequency domain (Silva, 1976; Krebes and Hron, 1981).

The Reservoir

For the applications, we consider a simple reservoir scenario based on the Sleipner field (North Sea). The reservoir rock is a high-porosity unconsolidated sandstone, the Utsira formation, which contains a large shallow saline aquifer. Due to its good storage capacity, carbon dioxide produced at this natural gas field has been injected into the Utsira sandstone since 1996 for sequestration purposes. A thick high-velocity layer, the Nørdland formation, overlies the sand acting as the caprock. In the particular case of Sleipner, it was established that the saturation model consists of two components: a main part of high CO_2 saturation trapped beneath the reservoir caprock or intrareservoir permeability barriers and a second component, of lower saturation, dispersed between the layers (Chadwick et al., 2005; Arts et al., 2004). According to the scheme used for the matrix propagator method, the upper half-space of our model represents the caprock and the lower half-space consists of the brine saturated Utsira sandstone. Below the caprock, the injected carbon dioxide is assumed to form in the sandstone a transition zone of thickness h, represented by a set of 40 layers of decreasing CO_2 saturation with depth, given by $S_{CO_2}(z)$. This is illustrated in Figure 1.

Carbon dioxide density and bulk modulus are calculated at the temperature of 36°C and the pressure of 10 MPa, to simulate the supercritical conditions of the injected CO_2 at Sleipner. The brine parameters are taken from Chadwick et al. (2005). These fluid properties are given in Table 1.

To calibrate our rock-physics model for the Utsira sandstone, we use its measured bulk density, the P- and S-wave velocities, an average porosity of 0.37, a mineral grain density of 2.68 g/cm³, and the properties of brine. Then, we perform a Gassmann-inverse calculation to estimate the frame bulk and shear modulus of 2.67 GPa and 0.857 GPa, respectively. The velocities and bulk density of the caprock and the sandstone are shown in Table 2. As stated previously, a velocity average between the homogeneous and patchy fluid mixtures is used within the transition layer (except where otherwise indicated).

In Figure 2, we show the Gassmann-Hill average P-wave velocity, the density, and acoustic impedance I_p versus depth. In this plot, carbon dioxide saturation is 100% below the caprock and decreases linearly to 0% at a depth $h = 50$ m, giving a CO_2 bulk saturation of 50%. All curves show a step change at the top of the transition layer, as a result of the contrast between the caprock and the CO_2-saturated sandstone. Then, the transition zone develops a continuous variation in the parameters that ends when the free CO_2 sandstone half-space is reached. The P-wave velocity inside the transition varies from 1420 m/s (for $S_{CO_2} = 100\%$) to 2050 m/s (for $S_{CO_2} = 0\%$), in agreement with Chadwick et al. (2005). The
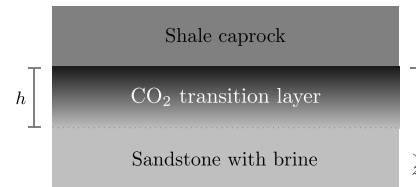

Figure 1. A CO_2 transition layer of thickness h encased between a shale and a brine-saturated sandstone half-spaces. The shading represents the CO_2 distribution that decreases with depth z.

Table 1. Reservoir fluid properties. CO_2 parameters are calculated according to the Peng and Robinson (1976) equation of state for $T = 36$°C and $P = 10$ MPa. Brine parameters are from Chadwick et al. (2005).

Fluid	ρ (kg/m³)	Bulk modulus (GPa)
CO_2	640	0.022
Brine	1040	2.305

Table 2. Rock properties of the reservoir. The sandstone parameters are at the pre-injection conditions.

Rock	ρ (kg/m³)	V_P (m/s)	V_S (m/s)
Shale caprock	2100	2270	850
Utsira sandstone	2073	2050	643

bulk density of the sandstone ρ_b also increases, but its total variation is not as marked as in the velocity. The same holds for the P-wave impedance.

AVA AND AVF ANALYSIS

Having defined the reservoir model, we begin the AVA/AVF sensitivity analysis of the resulting reflectivity from the reservoir with a CO_2 transition layer, according to the modeling procedure previously explained. The parameters, from which we will study their influence on the reflectivity $R_{pp}(f, \theta)$, are the transition layer thickness h, the bulk CO_2 saturation $\bar{S}$, and the type of fluid mixture.

The influence of thickness

The vertical scale lengths in a layered medium provide physical constraints on the behavior of the propagating waves. So, as our first test, we analyze the sensitivity to changes in h, assuming a saturation $\bar{S} = 50\%$. For a dominant frequency of 50 Hz and the velocity profile shown in Figure 2, the P-wavelengths λ_p are in the range of 28.4 to 41 m. For the same frequency, the wavelength in the caprock is 45.4 m. For this experiment, we consider thicknesses h that are greater and lower than those wavelengths.

In Figure 3a and 3b we compare the AVA response for transitions of thicknesses $h = 10, 25$, and 50 m. In the three cases, the real part of the P-wave generalized reflectivity is negative. This can be correlated with the decrease in acoustic impedance below the caprock, showing a behavior similar to an AVA class III, according to the standard classification.

Because, at low angles, the real parts of R_{pp} do not fluctuate around zero and the imaginary parts (shown in Figure 3b) are rather constant, the phase changes introduced by the transitions are almost independent of the incidence angle.

The reflectivity of the thin transitions ($h < \lambda_p$), corresponding to $h = 10$ and 25 m, are clearly different from that of the thick case ($h = 50$ m). The interference effects in these cases result in a strong reflection coefficient. However, the AVA curves are not very sensitive to the transition thickness, particularly for small incidence angles. This lack of sensitivity can be related to the analysis in Wolf (1937) and Justice and Zuba (1986), who noted the difficulties in the detection of a stratification when wavelengths are too long compared to total thickness.

For the thick transition case ($h > \lambda_p$) of $h = 50$ m, we observe in Figure 3a that, although the CO_2 transition zone will be seismically resolved, the real part of R_{pp} has a lower absolute value.

The AVF in Figure 3c and 3d manifests a sinc character similar to that expected from linear transition layers (Wolf, 1937; Justice and Zuba, 1986), but without the exponential decay at high frequencies (Liner and Bodmann, 2010).

Although the AVA response in the near offset for the thin transitions are rather similar, when we consider their reflectivity character versus frequency, thickness effects become evident: the AVF curves show a marked distinctive period for these layers. Whereas for thin thicknesses the lobes in Figure 3c and 3d are wide, as thickness increases, the AVF becomes highly oscillating within the seismic range and the peaks shift toward the low frequencies; this effect is also present in linear-velocity transition layers (Liner and Bodmann, 2010). The oscillatory character in R_{pp} is due to the complex exponential dependence of the propagator matrix coefficients with frequency, thickness, and velocity, which, for each layer k that comprise the transition zone, has the explicit form $e^{2\pi i f h_k / V_P^k}$. The periodicity of these factors explains the inverse proportionally in the position of peaks with thicknesses. This behavior may induce some ambiguity in the results because, for some combinations of frequency and thickness, similar reflectivities are observed.

An estimation of the transition thickness can be obtained, as plotted in Figure 4, if we take the modulus of R_{pp} from Figure 3c and 3d and relate the frequency f_{max}, for which $|R_{pp}(f)|$ is maximum, with h. We can see that, for thin layers, this frequency clearly follows the transition thickness. As thickness increases over $h = 50$ m, the relation becomes more ambiguous.

In what follows, we will consider the transition zone to be 50-m thick so as to satisfy $\lambda_p < h$ everywhere in the reservoir, to make sure that the transition will be seismically resolved. Next, we will study the effects of CO_2 content $\bar{S}$ and the type of mixture within the reservoir brine.
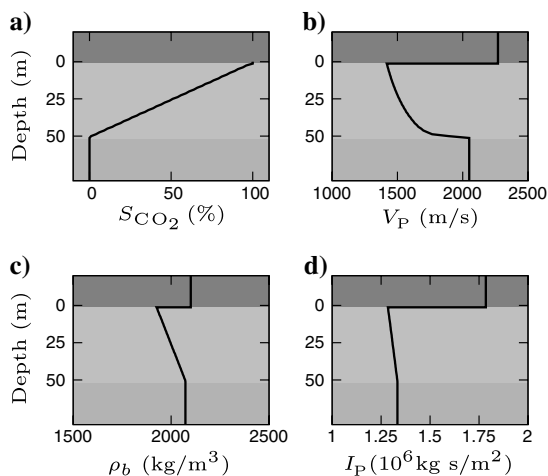

Figure 2. (a) CO_2 saturation, (b) P-wave velocity, (c) bulk density ρ_b, and (d) acoustic P-wave impedance I_P versus depth in the reservoir. Carbon dioxide saturation is 100% in the caprock/sandstone contact ($z = 0$) and decreases linearly to 0% at $z = 50$ m, giving $\bar{S} = 50\%$.
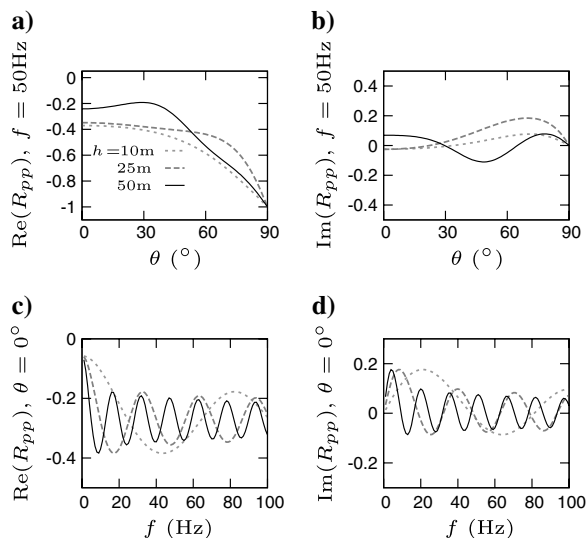

Figure 3. Effects of transition layer thickness on AVA (a and b) and AVF (c and d) for $\bar{S} = 50\%$.

The effect of CO$_2$ bulk saturation and fluid mixture type

In Figure 5, we show the effects related to the total amount of CO$_2$ $\bar{S}$, within the transition layer. The presence of carbon dioxide is readily evident when comparing the response to the pre-injection case $\bar{S} = 0\%$. As we can see in Figure 5a and 5b, for the 50-Hz frequency component, the effects of changing CO$_2$ saturation in AVA are not pronounced for angles below 45°. In Figure 5c and 5d, we plot the AVF oscillatory behavior, which clearly shows the effect of bulk saturation, particularly on the real part.

The slight change of AVA trend observed in Figure 5a at low angles can be used as a rough indicator of the overall saturation. Also, the AVA curve for $\bar{S} = 10\%$ shows a maximum at an angle near 60°, which shifts close to 30° for $\bar{S} = 50\%$. For large angles, the real part of the reflection coefficient becomes more negative as saturation increases.
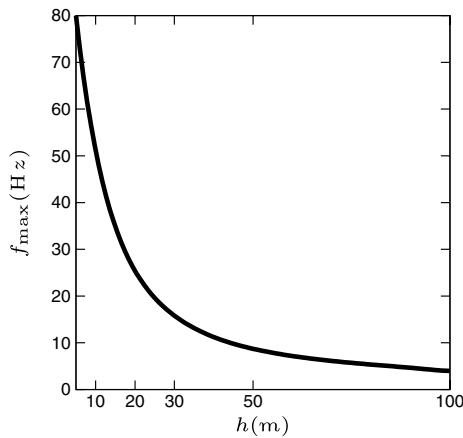
Small phase variation with angle will occur on the 50-Hz frequency component, because both real and imaginary parts of R_{pp}, shown in Figure 5a and 5b, behave in a similar fashion to those in Figure 3. As expected, when $\bar{S} = 0\%$, the transition zone vanishes and the reflection coefficient becomes real, taking the values given by the classic Zoeppritz (1919) solution for two half-spaces.

When inspecting Figure 5c, it is interesting to note that the mean value of the real part of R_{pp}, $\langle \mathrm{Re}\{R_{pp}(f)\} \rangle$, for frequencies in the range 0–100 Hz, can be used as a measure of the bulk CO$_2$ saturation in the transition zone. This is shown in Figure 6, where the average of the imaginary part is also given. As can be seen from Figure 3c and 7c, this measure is rather independent of the transition thickness and its fluid mixture type. For each overall saturation, we

Figure 4. The frequency $f_{\max}$, at which $|R_{pp}(f, \theta = 0°)|$ is maximum, as a function of transition thickness h. The transition has $\bar{S} = 50\%$.
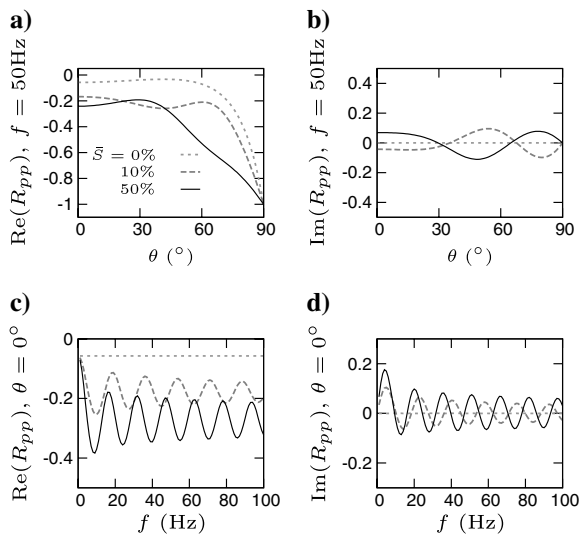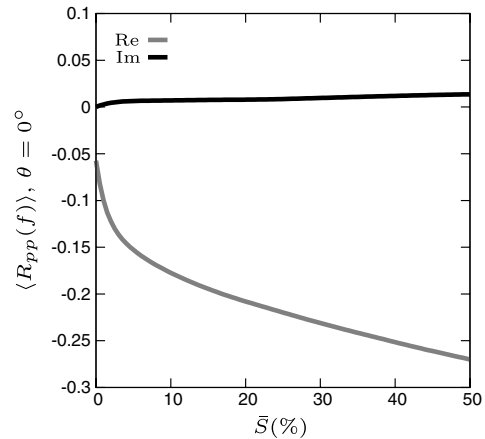
Figure 6. The mean value (over the real and imaginary parts) of $Rpp(f, \theta = 0°)$ between 0 and 100 Hz and its dependence on the transition CO$_2$ bulk saturation $\bar{S}$. The transition has $h = 50$ m.

Figure 5. Effect of bulk CO$_2$ saturation on AVA (a and b) and AVF (c and d) for $h = 50$ m.
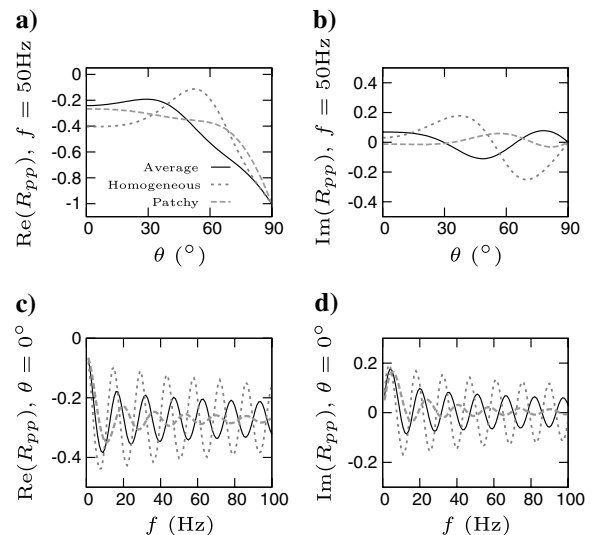
Figure 7. Fluid mixture response on AVA at 50 Hz (a and b) and AVF at normal incidence (c and d) for the $\bar{S} = 50\%$ and $h = 50$ m CO$_2$ transition layer for homogeneous or patchy fluid distributions. The result from averaging the velocity from both mixtures is also shown.

found that the frequency average $\langle \mathrm{Re}\{R_{pp}(f)\} \rangle$ tends to the Zoeppritz reflection coefficient associated with the contact of the caprock and the top of the transition layer, which, in turn, is its high-frequency limit.

Figure 7 demonstrates that the differences in reflectivity as a result of fluid distribution type are important. The patchy mixtures present lower AVF amplitudes, stronger frequency decay, and gentler AVA curves than the homogeneous mixture or the average saturation model. This behavior is a result of the differences in the velocity-saturation profile, which for the patchy limit decays rather linearly with CO_2 saturation. For this case, the velocity variation is similar to a Wolf ramp, which explains the similarity in their AVF, as can be observed by comparing Figure 7c and 7b.

For frequencies under 10 Hz, due to their long wavelengths, the AVF curves in Figures 5, 7, 8c, and 8d are rather similar. As expected, for $f = 0\,\mathrm{Hz}$ ($\lambda_p \to \infty$), the AVF curves converge into the normal incidence reflection coefficient at an equivalent interface between the caprock and the fully brine-saturated sandstone.

To complete the characterization of the CO_2 accumulation, we investigate how different the reflectivity response of the transition layer is to that of a constant CO_2 saturation and to the classical Wolf ramp.

Comparative analysis

To address the sensitivity of the normal incidence reflectivity to the velocity-depth profile, we again consider the transition layer of thickness $h = 50$ m and $\bar{S} = 50\%$ for a linear saturation profile with fluid distribution given as the average between the homogeneous and patchy limits (shown in Figure 2). In this section, we compare its response with a constant saturation case (where $S_{CO_2}(z) = \bar{S}$) and a Wolf ramp, for which an analytical closed-form expression of the normal incidence reflection coefficient can be derived (equation A-6).

As we can see in Figure 8a and 8b, the AVA response R_{pp} of the CO_2 stratification is clearly different from that of a constant satura-

tion zone with the same bulk saturation, hereafter denoted as R_{pp}^c. The monotonous change of the physical parameters between the transition zone generates a smoother, lower amplitude AVA behavior in the real and imaginary parts of R_{pp} when compared to the constant CO_2 case. In the frequency domain, we observe in Figure 8c and 8d that the real and imaginary parts of the normal incidence R_{pp} show an amplitude decay not present in R_{pp}^c. We also note that R_{pp} mimics the characteristic ringing of the reflection coefficient for a finite layer at low frequencies.

To compare the AVF response of the CO_2 saturation transition with that resulting from Wolf's (1937) analytical solution, Figure 9 presents the reflectivity that would result by assuming two possible linear-velocity models. For brevity, only the real parts are shown.

In the first approach, shown in Figure 9a, the Wolf ramp linearly connects the velocities of the shale caprock (upper half-space) with that of brine-saturated Utsira sandstone (lower half-space). By doing so, the velocity profile induced by the CO_2, which also has a different trend, is completely ignored. Thus, the modeled reflectivity is far different from that expected for the reservoir and obviously is not a reasonable procedure.

In the second approach, shown in Figure 9b, we consider a model in which the upper half-space has the same properties of the top of the transition layer (i.e., $S_{CO_2}(0) = 100\%$). In this case, as the Wolf ramp connects the velocity of the full CO_2-saturated sandstone to the fully brine-saturated sandstone, it shares the same trend as that of the nonlinear transition. As we can see, the Wolf ramp solution in this case, which includes information about the CO_2 transition (but none of the caprock), gives a better approximation of the reflectivity within the CO_2 zone. Both real parts show the sinc-like oscillations expected from linear transition layers. The amplitude decay with frequency and the placement of the notches are different. Because the frequency decay of reflectivity in the CO_2 transition is not exponential as is the case of Wolf ramps (Wolf, 1937; Liner and Bodmann, 2010), the effect of the CO_2 transition will be present at a wider frequency band.

In this section, we have seen that the periodicity in the AVF from the CO_2 transition resembles that of a constant CO_2 layer and the amplitude attenuation of a Wolf ramp. However, the complete characterization of the transition AVF is not captured by either of these simplifications.

These results allows us to conclude that detection methods based on recognition of the AVF signatures of classical linear-velocity transition zones, as applied by Liner and Bodmann (2010), would
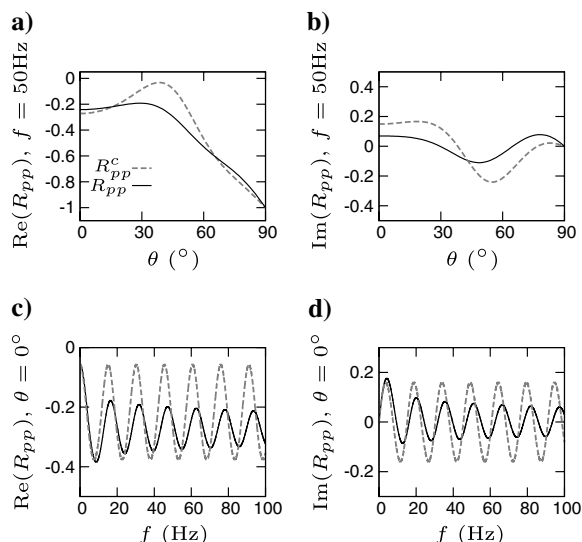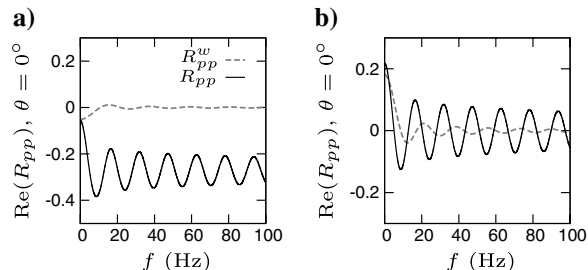
Figure 8. AVA and AVF response for the real (left) and imaginary (right) parts of the complex reflection coefficient for the 50-m transition layer, R_{pp}, and a constant CO_2-saturated zone R_{pp}^c of the same thickness. The CO_2 bulk saturation is 50% in both cases.

Figure 9. AVF response of the real part of the complex normal-incidence reflection coefficient for the $h = 50$ m, $\bar{S} = 50\%$ transition, R_{pp} layer, and a linear-velocity transition layer (Wolf ramp) R_{pp}^w, in the case when the caprock is taken as the first half-space (a) and when the first half-space is the top of the transition zone (b).
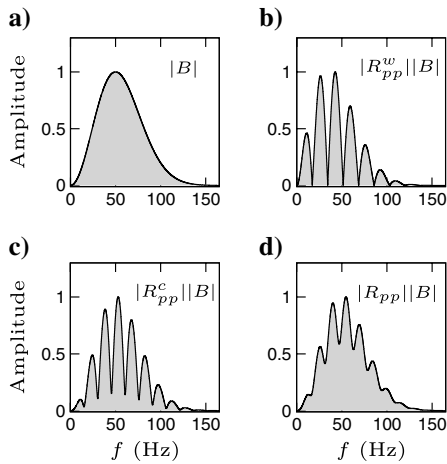
Figure 10. Normalized amplitude spectra resulting from a normal-incidence Ricker wavelet with spectrum B (a) reflected from the reservoir with (b) a Wolf ramp R_{pp}^w with the top of the transition layer as the reservoir upper half-space, (c) a constant CO_2 layer R_{pp}^c, and (d) the nonlinear saturation transition layer R_{pp}.

have to be modified for CO_2 transition layers where velocity varies in a nonlinear fashion.

Finally, to illustrate more clearly the effect of the different reflectivity models on the amplitude spectrum of reflected wavefields, given by the product of the amplitude spectrum of a seismic source and the modulus of the complex reflection coefficient (Justice and Zuba, 1986), we consider the amplitude spectrum $|B(f)|$ of an incident Ricker wavelet, given by (Zhang and Ulrych, 2002)

$$B(f) = \frac{2}{\sqrt{\pi}} \left(\frac{f}{f_m} \right)^2 \exp \left(-\frac{f^2}{f_m^2} \right), \qquad (5)$$

for a dominant frequency $f_m = 50$ Hz. In Figure 10, we compare the spectra resulting from the constant CO_2 zone, the Wolf ramp, and the transition layer considered in this section. The plots have been appropriately scaled to better display the changes.

We see that the amplitude modifications on the incident wavelet spectrum of Figure 10a, caused by the Wolf ramp in Figure 10b, are much more evident than the ones produced by the constant saturation and the transition models. In these graphs, we observe that the Wolf ramp behaves as a notch filter rejecting the reflection of several frequencies within the seismic range. We also find that the peak frequency component of the incident Ricker wavelet is shifted to lower frequencies, in agreement with Justice and Zuba (1986). These effects are not observed in Figure 10c and 10d. Thus, the transition layer shows the minimum amplitude distortion on the incident wavelet, followed closely by the constant CO_2 layer.

CONCLUSIONS

We have presented a parametric study of the generalized seismic reflectivity versus AVA and AVF, for a simple CO_2 storage scenario including a carbon dioxide saturation transition layer. For the different cases analyzed, we remark that

1) Discrimination between thin and thick CO_2 zones (with respect to the seismic wavelengths) seems feasible because of the distinct features of the associated AVF curves. However, the identification of thicknesses would be more likely when they

are smaller than the wavelengths because of the higher sensitivity of the generalized reflectivity in that case.

2) Bulk CO_2 saturation simultaneously affects the AVA and AVF response. Although the presence of CO_2 in the reservoir is clearly detected, with regards to the pre-injection case, a loss of sensitivity to track further changes in the CO_2 transition content is expected as CO_2 saturation increases. The frequency average of the real part of the reflectivity in the seismic range shows a good correlation with the overall CO_2 saturation present in the reservoir and is somewhat independent of the transition thickness and its fluid mixture type.

3) Characterization of fluid mixture with the aid of AVA and AVF seems theoretically feasible. The type of fluid mixture has an important influence in the amplitude and frequency dependence of reflectivity.

4) Modeling of CO_2 saturation transitions using the classical Wolf ramp formulation or equivalent constant saturation layers will fail to capture the complete character of their AVF signature.

5) The peak amplitude spectrum of a wavelet reflected at a linear saturation transition does not suffer the shift to low frequencies nor the Notch-type frequency filtering characteristic of Wolf ramps. Its spectrum is closer to that of a constant CO_2 layer with the same CO_2 bulk saturation.

These results lead us to the conclusion that the characterization of CO_2 transition zones for detection/monitoring purposes can be achieved with AVA and AVF analysis. The transition's bulk carbon dioxide saturation, fluid mixture, and thickness are easier to characterize by means of the AVF response.

We note that this kind of reflectivity analysis is not limited to the linear saturation-depth model used in this work and can be extended to any arbitrary saturation profile, as long as it can be discretized in a finite number of constant saturation layers.

The modeling and analysis of the time-domain and time-frequency variations associated with changes in the different parameters of the transition layer are topics of ongoing research, with the aim of assessing whether a detailed time-lapse monitoring and characterization of these zones can be pursued.

ACKNOWLEDGMENTS

APPENDIX A

THE REFLECTION COEFFICIENT OF A LINEAR TRANSITION ZONE

Although the expression of the normal-incidence reflection coefficient of a linear-velocity, constant density transition layer are shown in the works of Wolf (1937) and Liner and Bodmann (2010), we believe that it is adequate to put the full derivation that leads to the results in this work for two reasons: first, to reinforce future references about the topic of transition layers in geophysics and second, to correct some misspelled equations in the work of Liner and Bodmann (2010), which can lead to confusion if a direct application of the formulas is needed.

We will obtain, with respect to a space-fixed coordinate system, the normal incidence, frequency-dependent reflection, and transmission coefficients for a linear-velocity, constant density transition zone (Wolf ramp) that connects an upper medium of velocity v and

a lower medium of velocity kv with $k > 0$. The velocity in the transition is given by

$$V(z) = v\left(1 + \frac{k-1}{h}z\right) \qquad (A-1)$$

for z in $0 < z < h$, where z is depth and h is the transition thickness. The coordinate system has the positive z-direction into the transition zone and has its zero at the top of the transition (see Figure 1).

The Fourier transform of the displacement $\hat{u}(z, \omega)$ that satisfies the wave equation in the frequency domain, can be written in the half-spaces, and is in the transition layer (Appendix B) as

$$\begin{cases} \hat{u}_{\mathrm{u}}(z,\omega) = e^{-\frac{i\omega z}{v}} + \mathcal{R}e^{+\frac{i\omega z}{v}}, & z \leq 0; \\ \hat{u}_{\mathrm{tl}}(z,\omega) = CV(z)^{m_1} + DV(z)^{m_2}, & 0 < z < h; \quad (A-2) \\ \hat{u}_{\mathrm{d}}(z,\omega) = \mathcal{T}e^{-\frac{i\omega(z-h)}{kv}}, & z \geq h; \end{cases}$$

where m_1 and m_2 are given by $m_{1,2} = -\frac{1}{2} \pm \gamma(f)$, with $\gamma(f) = \sqrt{\frac{1}{4} + \sigma^2(f)}$ and $\sigma(f) = \frac{i\omega h}{(k-1)v}$; where $i = \sqrt{-1}$, $\omega = 2\pi f$, and f is the frequency. The reflection coefficient $\mathcal{R}$, the transmission coefficient $\mathcal{T}$, C, and D are complex. The subscript u denotes the upper half-space, the subscript tl denotes the transition layer, and d denotes the lower half-space. By applying the continuity of $\hat{u}$ and $\partial\hat{u}/\partial z$ at the top of the transition layer ($z = 0$) and at the bottom ($z = h$), we move to the set of equations,

$$\begin{cases} 1 + \mathcal{R} & = & C + D \\ \sigma(\mathcal{R} - 1) & = & Cm_1 + Dm_2 \\ \mathcal{T} & = & Ck^{m_1} + Dk^{m_2} \\ -\sigma\mathcal{T} & = & Cm_1 k^{m_1} + Dm_2 k^{m_2} \end{cases} \qquad (A-3)$$

As a next step, by simple multiplication and addition of the previous equations we can write a system involving only the transition layer coefficients,

$$\begin{cases} C(\sigma - m_1) + D(\sigma - m_2) & = & 2\sigma \\ Ck^\gamma(\sigma + m_1) + Dk^{-\gamma}(\sigma + m_2) & = & 0 \end{cases} \qquad (A-4)$$

Solving for C and D and using the identity $k^\gamma = e^{\gamma \ln k}$ to write the results in terms of hyperbolic trigonometric functions, we obtain for $k \neq 1$,

$$\begin{aligned} C &= -\frac{(\sigma+m_2)k^{-\gamma}}{2\sigma \sinh(\gamma \ln k)+2\gamma \cosh(\gamma \ln k)}, \\ D &= \frac{(\sigma+m_1)k^{\gamma}}{2\sigma \sinh(\gamma \ln k)+2\gamma \cosh(\gamma \ln k)}. \end{aligned} \qquad (A-5)$$

Then, with the aid of the first equation in A-3, the frequency-dependent reflection coefficient for the transition layer can be written as

$$\mathcal{R} = -\frac{1}{2\sigma + 2\gamma \coth(\gamma \ln k)}. \qquad (A-6)$$

Finally, using the third equation in A-3, the displacement transmission coefficient is

$$\mathcal{T} = \frac{2\gamma k^{-1/2}}{2\sigma \sinh(\gamma \ln k) + 2\gamma \cosh(\gamma \ln k)}. \qquad (A-7)$$

As a final remark, we recall that the reflection coefficient R (R_{pp}^w in this work), which appears in Wolf (1937) and Liner and Bodmann (2010), is the reflection coefficient for potential amplitude R, which is related to the displacement reflection coefficient $\mathcal{R}$ by $R = -\mathcal{R}$ (Sheriff, 1991; Lay and Wallace, 1995; Mavko et al., 2011)

APPENDIX B

WAVE EQUATION IN A LINEAR TRANSITION LAYER

We will solve the wave equation on a linear-velocity transition layer,

$$\frac{\partial}{\partial z}\left(V^2(z)\frac{\partial u}{\partial z}\right) = \frac{\partial^2 u}{\partial t^2}, \qquad (B-1)$$

for $u(z, t)$ with z in $0 < z < h$ and $V(z) = v(1 + \frac{k-1}{h}z)$. By means of the Fourier transform of the displacement with respect to time $u(z, t) \leftrightarrow \hat{u}(z, w)$, the previous differential equation becomes

$$\frac{\partial}{\partial z}\left(V^2(z)\frac{\partial \hat{u}}{\partial z}\right) + \omega^2 \hat{u} = 0, \qquad (B-2)$$

where $w = 2\pi f$ is the angular frequency and f is the frequency. Performing the spatial derivatives gives

$$2\frac{v(k-1)}{h}V\frac{\partial \hat{u}}{\partial z} + V^2\frac{\partial^2 \hat{u}}{\partial z^2} + \omega^2 \hat{u} = 0. \qquad (B-3)$$

Solutions to equation B-3 are of the type,

$$\hat{u}(z,\omega) = V^m(z) = \left[v\left(1 + \frac{k-1}{h}z\right)\right]^m, \qquad (B-4)$$

where m is a complex number. Inserting equation B-4 into B-3 yields

$$\left[m(m+1) + \frac{\omega^2 h^2}{(k-1)^2 v^2}\right]V^m(z) = 0. \qquad (B-5)$$

Following Wolf (1937) notation, if $\sigma(f) = i\omega h/(k-1)v$ and $\gamma(f) = \sqrt{\frac{1}{4} + \sigma^2(f)}$ with $i = \sqrt{-1}$, the parameters m_1 and m_2 that satisfy equation B-5 are given by $m_{1,2} = -\frac{1}{2} \pm \gamma$.

A general solution on the transition layer in the frequency-space domain can be expressed as a linear combination of the base solutions:

$$\hat{u}(z,\omega) = CV(z)^{m_1} + DV(z)^{m_2}, \qquad (B-6)$$

where C and D are complex.

REFERENCES

Arts, R., O. Eiken, A. Chadwick, L. van der Meer, and B. Zinszner, 2004, Monitoring of CO_2 at Sleipner using time-lapse seismic data: Energy, **29**, 1383–1392, doi: 10.1016/j.energy.2004.03.072.

Batzle, M., and Z. Wang, 1992, Seismic properties of pore fluids: Geophysics, **57**, 1396–1408, doi: 10.1190/1.1443207.

Berryman, L. H., P. L. Goupillaud, and K. H. Waters, 1958, Reflections from multiple transition layers. Part I — Theoretical results: Geophysics, **23**, 223–243, doi: 10.1190/1.1438461.

Bortfeld, R., 1960, Seismic waves in transition layers: Geophysical Prospecting, **8**, 178–217, doi: 10.1111/gpr.1960.8.issue-2.

Brekhovskik, L. M., 1980, Waves in layered media, 2nd. ed.: Academic.

Chadwick, R. A., R. Arts, and O. Eiken, 2005, 4D seismic quantification of a growing CO₂ plume at Sleipner, North Sea: Petroleum Geology: North-West Europe and Global Perspectives-Proceedings of the 6th Petroleum Geology Conference, 1385–1399.

Chadwick, R. A., D. Noy, E. Lindeberg, R. Arts, O. Eiken, and G. Williams, 2006, Calibrating reservoir performance with time-lapse seismic monitoring and flow simulations of the Sleipner CO₂ plume: 8th International Conference on Greenhouse Gas Control Technologies.

Dutta, N., and H. Odé, 1979, Attenuation and dispersion of compressional waves in fluid-filled porous rocks with partial gas saturation (White model). Part I: Biot theory: Geophysics, **44**, 1777–1788, doi: 10.1190/1.1440938.

Gassmann, F., 1951, Über die Elastizität poröser Medien: Vierteljahrschrift der Naturforschenden Gessellshaft in Zurich, **96**, 1–23.

Gupta, R. N., 1966, Reflection of plane elastic waves from transition layers with arbitrary variation of velocity and density: Bulletin of the Seismological Society of America, **56**, 633–642.

Justice, J. H., and C. Zuba, 1986, Transition zone reflections and permafrost analysis: Geophysics, **51**, 1075–1086, doi: 10.1190/1.1442163.

Krebes, E., and F. Hron, 1981, Comparison of synthetic seismograms for anelastic media by asymptotic ray theory and the Thomson-Haskell method: Bulletin of the Seismological Society of America, **71**, 1463–1468.

Lay, T., and T. C. Wallace, 1995, Modern global seismology: Academic Press.

Liner, C. L., and B. G. Bodmann, 2010, The Wolf ramp: Reflection characteristics of a transition layer: Geophysics, **75**, A31–A35, doi: 10.1190/1.3476312.

Mavko, G., and T. Mukerji, 1998, Bounds on low-frequency seismic velocities in partially saturated rocks: Geophysics, **63**, 918–924, doi: 10.1190/1.1444402.

Mavko, G., T. Mukerji, and J. Dvorkin, 2011, The rock physics handbook: Tools for seismic analysis of porous media, 2nd. ed.: Cambridge University Press.

Peng, D. Y., and D. R. Robinson, 1976, A new two-constant equation of state: Industrial and Engineering Chemistry Fundamentals, **15**, 59–64, doi: 10.1021/i160057a011.

Pride, S., J. Berryman, and J. Harris, 2004, Seismic attenuation due to wave-induced flow: Journal of Geophysical Research, **109**, B01201, doi: 10.1029/2003JB002639.

Rubino, J., C. Ravazzoli, and J. E. Santos, 2009, Equivalent viscoelastic solids for heterogeneous fluid-saturated porous rocks: Geophysics, **74** (1), N1–N13, doi: 10.1190/1.3008544.

Sheriff, R. E., 1991, Encyclopedic dictionary of exploration geophysics: SEG.

Silva, W., 1976, Body waves in layered anelastic solid: Bulletin of the Seismological Society of America, **66**, 1539–1554.

Tsvankin, I., 1995, Seismic wavefields in layered isotropic media: Samizdat Press.

White, D., 2009, Monitoring CO₂ storage during EOR at the Weyburn-Midale field: The Leading Edge, **28**, 838–842, doi: 10.1190/1.3167786.

Wolf, A., 1937, The reflection of elastic waves from transition layers of variable velocity: Geophysics, **2**, 357–363, doi: 10.1190/1.1438104.

Wuenschel, P. C., 1960, Seismogram synthesis including multiples and transmission coefficients: Geophysics, **25**, 106–129, doi: 10.1190/1.1438677.

Zhang, C., and T. J. Ulrych, 2002, Estimation of quality factors from CMP records: Geophysics, **67**, 1542–1547, doi: 10.1190/1.1512799.

Zoeppritz, K., 1919, On the reflection and propagation of seismic waves: Göttinger Nachrichten, **1**, 66–84.